Monthly Notices
of the
ROYAL ASTRONOMICAL SOCIETY

MNRAS **450,** 3319–3330 (2015) doi:10.1093/mnras/stv797

Voids in modified gravity reloaded: Eulerian void assignment

Tsz Yan Lam,[1] Joseph Clampitt,[2⋆] Yan-Chuan Cai[3] and Baojiu Li[3]

[1]*Max Planck Institute for Astrophysics, Karl-Schwarzschild-Str. 1, D-85748 Garching, Germany*
[2]*Center for Particle Cosmology, Department of Physics and Astronomy, University of Pennsylvania, 209 S. 33rd St, Philadelphia, PA 19104, USA*
[3]*Institute for Computational Cosmology, Department of Physics, Durham University, South Road, Durham DH1 3LE, UK*

Accepted 2015 April 9. Received 2015 March 16; in original form 2014 August 21

ABSTRACT

We revisit the excursion set approach to calculate void abundances in chameleon-type modified gravity theories, which was previously studied by Clampitt, Cai & Li. We focus on properly accounting for the void-in-cloud effect, i.e. the growth of those voids sitting in overdense regions may be restricted by the evolution of their surroundings. This effect may change the distribution function of voids hence affect predictions on the differences between modified gravity (MG) and general relativity (GR). We show that the thin-shell approximation usually used to calculate the fifth force is qualitatively good but quantitatively inaccurate. Therefore, it is necessary to numerically solve the fifth force in both overdense and underdense regions. We then generalize the Eulerian-void-assignment method of Paranjape, Lam & Sheth to our modified gravity model. We implement this method in our Monte Carlo simulations and compare its results with the original Lagrangian methods. We find that the abundances of small voids are significantly reduced in both MG and GR due to the restriction of environments. However, the change in void abundances for the range of void radii of interest for both models is similar. Therefore, the difference between models remains similar to the results from the Lagrangian method, especially if correlated steps of the random walks are used. As Clampitt et al., we find that the void abundance is much more sensitive to MG than halo abundances. Our method can then be a faster alternative to *N*-body simulations for studying the qualitative behaviour of a broad class of theories. We also discuss the limitations and other practical issues associated with its applications.

Key words: methods: numerical – cosmology: theory – dark energy – large-scale structure of Universe.

1 INTRODUCTION

The discovery of the accelerated expansion of the Universe sparked a surge of research on the possibility of modified gravity models (see for example, Jain & Khoury 2010; Clifton et al. 2012, for reviews). The main goal of such modifications is to alter the large-scale behaviour to explain the acceleration – however, any modifications in the gravity model must at the same time satisfy the tight constraints from the Solar system tests. One way to fulfil this requirement is to include some kind of screening mechanism to suppress the modification in the local environment (i.e. regimes with high matter density or deep Newtonian potential). In this work, we focus on one particular subclass of modified gravity theories – one that modifies gravity by introducing a dynamical scalar field that mediates a fifth force.

The chameleon model of Khoury & Weltman (2004) is a very representative example of this class of modified gravity theories. In this model, the acceleration of the Universe is associated with a scalar field, which has a runaway-type self-interaction potential and an interaction (coupling) with matter. Such a specific setup ensures that during the cosmic evolution the scalar field is trapped to the vicinity of 0, so that its potential energy roughly stays as a constant – of the order of the energy density of the cosmological constant in the Λ cold dark matter (ΛCDM) paradigm – which means that the expansion history can be very close to that of ΛCDM. The coupling to matter produces a fifth force which can be as strong as standard gravity, so that the model is naively ruled out by Solar system tests of gravity. However, because the scalar field is trapped close to 0 (especially in regions with high matter density), the fifth force can be severely suppressed, thereby passing the stringent local constraints. This is the chameleon mechanism (Khoury & Weltman 2004), in which the behaviour of the fifth force depends on the environment: the suppression of the fifth force in the Solar system is achieved by reducing its force range to submillimetres, while on the cosmological background (at late times) the force range can be of the order of $\mathcal{O}$(1-10) Mpc, on which scales strong deviations from ΛCDM can be found. Notice that on even larger scales, the

⋆ E-mail: clampitt@sas.upenn.edu

effect of the fifth force diminishes, implying that the effect on very large-scale structures is minimal.

Because the background evolution and the linear perturbations on large scales can be indistinguishable from the standard ΛCDM cosmology (Hu & Sawicki 2007; Li & Barrow 2007; Li & Zhao 2009), and Solar system tests are satisfied by construction, non-linear structure formation (on scales of 10^0–10^2 Mpc) is the only regime where effects of such models would possibly be detected. A number of studies (e.g. Oyaizu 2008; Oyaizu, Lima & Hu 2008; Li & Zhao 2009, 2010; Schmidt et al. 2009; Li & Barrow 2011; Zhao, Li & Koyama 2011; Li et al. 2012a) employed *N*-body numerical simulations to study non-linear structure formation – however high-resolution simulations with cosmological volume are still challenging due to the highly non-linear equation governing the scalar field. As a result, semi-analytic methods are often used to make qualitative predictions and provide insights into the underlying physics for such models.

This work will be along this direction and aim at investigating the effect of the chameleon-type modified gravity (MG) on the large-scale structure in the non-linear regime. We will extend the standard excursion set approach (Bond et al. 1991; Mo & White 1996; Sheth & Tormen 1999) to predict the abundance of structures. The application of this approach to halo abundance and bias has been visited by Li & Efstathiou (2012), Li & Lam (2012) and Lam & Li (2012), and therefore in this work we will focus on cosmic voids.

Cosmic voids found in redshift surveys have many applications. Observationally, Hoyle, Vogeley & Pan (2012) studied the photometric properties of void galaxies found by Hoyle & Vogeley (2002) and Pan et al. (2012). There is also ongoing work towards using voids as cosmological probes. The Alcock–Paczynski test has been proposed (Lavaux & Wandelt 2012) and progress has even been made towards applying it to data (Sutter et al. 2012, 2014). Stacking of voids for the cosmic microwave background has been used to detect the integrated Sachs–Wolfe effect as an alternative to the cross-correlation method (Granett, Neyrinck & Szapudi 2008; Ilić, Langer & Douspis 2013; Planck Collaboration XIX 2014; Cai et al. 2014a,b; Hotchkiss et al. 2015); Void–void and void–galaxy clustering is another promising cosmological probe (Hamaus et al. 2014). Recent measurements of the weak lensing signal (Melchior et al. 2014) and density profile of voids (Clampitt & Jain 2014) gives a direct handle on their dark matter content. Void ellipticity has been shown to be sensitive to the dark energy equation of state (Bos et al. 2012). Voids properties have been studied in coupled dark energy model using *N*-body simulations (Li 2011; Sutter et al. 2015).

The excursion set predictions of void abundances have been done previously by Clampitt, Cai & Li (2013), where they showed that voids, due to the underdensity and therefore weaker suppression of the fifth force inside them, would yield a stronger signal of MG compared to haloes. This work focuses on applying a modern void-assignment algorithm, Eulerian void assignment, in the context of the same modified gravity model. Eulerian void assignment was recently proposed by Paranjape, Lam & Sheth (2012b) as an improvement to the traditional Lagrangian-based assignment by taking into account the effect of the immediate surroundings on the growth of voids.

This paper is organized as follows. In Section 2, we briefly review the theoretical model to be considered and summarize its main ingredients. In Section 3, we find and validate the numerical solutions to the fifth force, which will be used in Section 4 to calculate numerically the evolution of spherical over and underdensities in the modified gravity model. Section 5 presents a detailed description of the different void-assignment methods adopted in the literature and in this paper; in particular, we will describe how the Eulerian method of Paranjape et al. (2012b) can be implemented in the context of MG. In Section 6, we show the comparison of predictions on the void abundance from the different methods and demonstrate their consistency. Finally, Section 7 summarizes the main results and discusses their implications.

2 THE CHAMELEON THEORY

This section presents the theoretical framework for investigating the cosmological effects of a coupled scalar field. We will give the relevant general field equations in Section 2.1, and then specify the models analysed in this paper in Section 2.2.

2.1 Cosmology with a coupled scalar field

The equations governing the scalar field can be found in Li & Zhao (2009, 2010) and Li & Barrow (2011), and are presented here only to make this paper self-contained. Because of this, this section is brief and contains only the most essential ingredients of coupled scalar field cosmology. Interested readers are referred to the above references for more details.

We start from a Lagrangian density

$$\mathcal{L} = \frac{1}{2}\left[M_{\rm Pl}^2 R - \nabla^a\phi\nabla_a\phi\right] + V(\phi) - C(\phi)(\mathcal{L}_{\rm DM} + \mathcal{L}_{\rm S}), \quad (1)$$

in which R is the Ricci scalar, the reduced Planck mass is $M_{\rm Pl} = 1/\sqrt{8\pi G}$ with G being Newton's constant, and $\mathcal{L}_{\rm DM}$ and $\mathcal{L}_{\rm S}$ are, respectively, the Lagrangian densities for dark matter and standard model fields. ϕ is the scalar field and $V(\phi)$ is the potential describing its self-interaction. The coupling function $C(\phi)$, on the other hand, describes its interaction with matter. The coupled scalar field model is then fully specified by the functional forms for $V(\phi)$ and $C(\phi)$.

Varying the total action with respect to the metric g_{ab}, we obtain the following expression for the total energy momentum tensor in this model:

$$T_{ab} = \nabla_a\phi\nabla_b\phi - g_{ab}\left[\frac{1}{2}\nabla^c\nabla_c\phi - V(\phi)\right] + C(\phi)(T_{ab}^{\rm DM} + T_{ab}^{\rm S}),$$

where $T_{ab}^{\rm DM}$ and $T_{ab}^{\rm S}$ are the energy momentum tensors for (uncoupled) dark matter and standard model fields. The existence of the scalar field and its coupling change the form of the energy momentum tensor, leading to potential changes in the background cosmology and structure formation.

The coupling to the scalar field generates an extra interaction (the fifth force) between matter particles, which can be regarded as a result of the exchange of scalar quanta. This is best illustrated by the geodesic equation for dark matter particles

$$\frac{{\rm d}^2\boldsymbol{r}}{{\rm d}t^2} = -\nabla\Phi - \frac{C_\phi(\phi)}{C(\phi)}\nabla\phi, \quad (2)$$

where $\boldsymbol{r}$ is the particle position, t is the physical time, Φ is the Newtonian potential and ∇ is the spatial derivative; $C_\phi \equiv {\rm d}C/{\rm d}\phi$. The second term on the right-hand side is the fifth force, whose potential (the conservative force potential, not to be confused with the self-interacting potential $V(\phi)$) can be described by $\ln C(\phi)$.

Equation (2) suggests that to follow the motion of particles we need to know the time evolution and spatial configuration of ϕ. This is usually achieved by explicitly solving the scalar field equation of motion

$$\nabla^a\nabla_a\phi + \frac{{\rm d}V(\phi)}{{\rm d}\phi} + \rho\frac{{\rm d}C(\phi)}{{\rm d}\phi} = 0, \quad (3)$$

where $\rho = \rho_{\rm DM} + \rho_{\rm b}$ is the sum of dark matter and baryonic matter densities. Equivalently, the equation of motion can be written as

$$\nabla^a \nabla_a \phi + \frac{{\rm d}V_{\rm eff}(\phi)}{{\rm d}\phi} = 0, \tag{4}$$

where we have defined an effective potential for the scalar field

$$V_{\rm eff}(\phi) = V(\phi) + \rho C(\phi). \tag{5}$$

The background evolution of ϕ can be solved given the present-day value of $\bar{\rho}$ (note that $\bar{\rho} \propto a^{-3}$; Li & Zhao 2009). We can then split ϕ into two parts, $\phi = \bar{\phi} + \delta\phi$, where $\bar{\phi}$ is the background value of ϕ and $\delta\phi$ is its perturbation around $\bar{\phi}$, and subtract the background part of the scalar field equation of motion from the full equation to find the equation of motion for $\delta\phi$. In the quasi-static limit, where we can neglect all time derivatives of $\delta\phi$ compared with its spatial derivatives (this is a good approximation on scales well within the horizon), this can be obtained as

$$\nabla^2 \delta\phi = \frac{{\rm d}C(\phi)}{{\rm d}\phi}\rho - \frac{{\rm d}C(\bar{\phi})}{{\rm d}\bar{\phi}}\bar{\rho} + \frac{{\rm d}V(\phi)}{{\rm d}\phi} - \frac{{\rm d}V(\bar{\phi})}{{\rm d}\bar{\phi}}. \tag{6}$$

The calculation of the scalar field ϕ using the above equation then completes the source term of the Poisson equation,

$$\begin{aligned}\nabla^2\Phi &= \frac{1}{2M_{\rm Pl}^2}\left[\rho_{\rm tot} + 3p_{\rm tot}\right] - \frac{1}{2M_{\rm Pl}^2}\left[\bar{\rho}_{\rm tot} + 3\bar{p}_{\rm tot}\right] \\ &= \frac{1}{2M_{\rm Pl}^2}\left[\rho C(\phi) - \bar{\rho}C(\bar{\phi}) - 2V(\phi) + 2V(\bar{\phi})\right], \end{aligned} \tag{7}$$

where we have neglected the kinetic energy of the scalar field since the running of ϕ is always negligible for the model studied here. In equation (7), we have again exploited the quasi-static approximation by dropping time derivatives of the Newtonian potential.

2.2 Specification of model

As mentioned above, to completely specify the coupled scalar field model, we need to give the functional forms of $V(\phi)$ and $C(\phi)$. Here, for illustration purpose, we will use the chameleon-type models investigated by Li & Zhao (2009, 2010), with

$$C(\phi) = \exp(\gamma\phi/M_{\rm Pl}), \tag{8}$$

and

$$V(\phi) = \frac{\rho_\Lambda}{\left[1 - \exp\left(-\phi/M_{\rm Pl}\right)\right]^\alpha}. \tag{9}$$

In the above ρ_Λ is the energy density of the cosmological constant in the standard ΛCDM scenario, ϕ plays the role of dark energy in this model, and γ, α are dimensionless model parameters which control the strength of the coupling $C(\phi)$ and the slope of the scalar field self-interaction potential $V(\phi)$, respectively.

We choose $\alpha \ll 1$ and $\gamma > 0$ as in Li & Zhao (2009, 2010), so that the global minimum of $V_{\rm eff}(\phi)$ is always very close to $\phi = 0$ throughout the cosmic evolution, and that $m_\phi^2 \equiv {\rm d}^2 V_{\rm eff}(\phi)/{\rm d}\phi^2$ at this minimum is very large in high-density regimes. For example, the minimum of $V_{\rm eff}(\phi)$ on a background with matter density ρ is approximately (Li & Zhao 2009)

$$\phi = \frac{\alpha\rho_\Lambda}{\gamma\rho}, \tag{10}$$

such that $\phi \ll 1$, especially in high-density regions where $\rho \gg \rho_\Lambda$. Such choices of model parameters ensure that:

(i) ϕ is trapped in the vicinity of $\phi = 0$ throughout the cosmic history and thus $V(\phi) \approx \rho_\Lambda$ behaves as a cosmological constant. For this reason, we take the background expansion of this model to be exactly the same as that of ΛCDM with the same cosmological parameters. Note that this is not guaranteed if $\alpha \ll 1$ does not hold.

(ii) The fifth force is strongly suppressed in high-density regions where ϕ acquires a large mass, $m_\phi^2 \gg H^2$ (H is the Hubble expansion rate), and therefore the fifth force cannot propagate a long distance without decaying. This is because the fifth force, mediated by a scalar field, takes the Yukawa form and decays exponentially over the Compton wavelength, $\lambda \equiv m_\phi^{-1}$, of this scalar field.

The fact that the fifth force is strongly suppressed when matter density is high implies that its influence on structure formation occurs mainly at late times. The environment-dependent behaviour of the fifth force was first considered in Khoury & Weltman (2004), and has since then been known as 'chameleon screening'. It is one of the most well-studied modified gravity theories: because of the finite range of the fifth force, and because of the severe suppression of it in high-density regions, it is believed that the strongest cosmological constraints on such models come from the study of cosmic voids, which are low-density regions ($\delta \sim -0.8$) in the Universe with sizes ranging from a few to $\mathcal{O}(100)$ Mpc.

3 FORCE SOLUTIONS

Although in this work we are only concerned with void abundances, the Eulerian-void-assignment method of Paranjape et al. (2012b) requires solutions for collapsing overdense walls around the voids. Thus, the equations below will apply generally to calculate fifth forces for under *and* overdensities. The distinction between the two regimes is made entirely in the choice of parameters, specifically the ratio of the object's density to that of its environment. After presenting the general equations, we will focus on the overdense solutions since they are unique to this work (underdense solutions were already shown in detail in Clampitt et al. 2013). Finally, we will describe numerical checks of our algorithm.

3.1 Scalar field solution

We are interested in the simplest model of a dark matter halo (or void), with top-hat (or bucket) density profiles described by

$$\rho_0(\chi) = \begin{cases} \rho_{\rm in} & \text{for} \quad \chi \le r \\ \rho_{\rm out} & \text{for} \quad \chi > r \end{cases}, \tag{11}$$

in which r is the object's radius and χ is a variable characterizing the distance from the centre of the object. Because ϕ is confined to the vicinity of $\phi = 0$, we have $C(\phi) \approx 1$ and the first term on the right-hand side of equation (7) can be integrated once to find the force per unit test mass

$$F_{\rm N}(\chi) = -\frac{GM(<\chi)}{\chi^2}. \tag{12}$$

The second term on the right-hand side of equation (2) is the fifth force, which for our choice of $C(\phi)$ in equation (8) can be expressed as

$$F_\phi(\chi) = -\gamma\frac{\rm d}{{\rm d}\chi}(\phi/M_{\rm Pl}). \tag{13}$$

We define the ratio of fifth to Newtonian forces at the surface of the object ($\chi = r$) as

$$\eta \equiv \frac{F_\phi}{F_{\rm N}} = \frac{6\gamma M_{\rm Pl}}{r\rho_{\rm in}}\left.\frac{{\rm d}\phi}{{\rm d}\chi}\right|_{\chi=r}, \tag{14}$$

which is constrained to be $\eta \le 2\gamma^2$ for overdensities.

In the model considered in this work, the force ratio η can be equivalently determined by three length-scales: the radius of the object r, and the Compton wavelengths inside and outside the object. The latter are given by the following relations:

$$\rho_i = \left(\frac{M_{\rm Pl}\sqrt{\alpha\rho_\Lambda}}{\gamma}\right)\frac{1}{\lambda_i}, \tag{15}$$

where $i = [\text{in, out}]$ and λ is the Compton wavelength of the scalar field (note that the Compton wavelength is small on a high matter-density background and vice versa). In Clampitt et al. (2013), we showed that the degrees of freedom of a spherical top-hat under-density can be reduced from the three length-scales, r, $\lambda_{\rm in}$ and $\lambda_{\rm out}$, to two ratios of these lengths: $r/\lambda_{\rm out}$ and $\lambda_{\rm out}/\lambda_{\rm in}$. This logic proceeds without change for overdensities, and so we only quote the key equations here.

The effective potential for the specific model studied here can be written as

$$V_{\rm eff}(\phi) = \frac{\Lambda}{\left[1-\exp\left(-\phi/M_{\rm Pl}\right)\right]^\alpha} + \rho_i \exp(\gamma\phi/M_{\rm Pl})\,, \tag{16}$$

with which the equation of motion equation (4) can be simplified to read

$$\frac{{\rm d}^2\psi}{{\rm d}\tau^2} + \frac{2}{\tau}\frac{{\rm d}\psi}{{\rm d}\tau} + \frac{1}{\psi} = \begin{cases} \lambda_{\rm out}/\lambda_{\rm in} & \text{for} \quad \tau \le r/\lambda_{\rm out} \\ 1 & \text{for} \quad \tau > r/\lambda_{\rm out} \end{cases} \tag{17}$$

with the following two boundary conditions:

$$\left.\frac{{\rm d}\psi}{{\rm d}\tau}\right|_{\tau=0} = 0, \qquad \psi(\tau\to\infty) = 1\,. \tag{18}$$

Note that in the above the solution has been rescaled and written in terms of $\psi \equiv \phi/\phi_{\rm out}$ and $\tau \equiv \chi/\lambda_{\rm out}$. Rewriting equation (14) in terms of the new variables and using $\rho_\Lambda = \Omega_\Lambda\rho_{\rm c}$ (where $\rho_{\rm c}$ is the critical density at the present day), we find

$$\eta(r) = 6\gamma\sqrt{\frac{\alpha\Omega_\Lambda}{\Omega_{\rm m}}}\frac{M_{\rm Pl}\sqrt{\bar\rho_{\rm m}}}{r\rho_{\rm in}}\left.\frac{{\rm d}\psi}{{\rm d}\tau}\right|_{\tau=r/\lambda_{\rm out}}, \tag{19}$$

where $\bar\rho_{\rm m}$ is the background matter density today.

The recasting of the scalar field equation of motion in the form of equation (17) has the advantage that the fifth-force-to-gravity ratio $\eta(r)$ can then be obtained by interpolating a 2D pre-computed table, for spherical top-hat systems of arbitrary size, density, and in any kind of environment. This can in turn greatly simplify the numerical computations in this work, which would otherwise be prohibitively expensive.

3.2 Comparison to the thin-shell approximation

The radial profile of a chameleon-type scalar field has been studied in detail for spherical overdensities (see e.g. Khoury & Weltman 2004; Davis et al. 2012; Lombriser et al. 2012, for a few examples). Khoury & Weltman (2004) derived a simple analytical formula for the fifth force which has been shown to agree well with numerical simulations (Li, Zhao & Koyama 2012b). Here we show that the thin-shell prescription followed by Li & Efstathiou (2012, rewritten using our reduced parameters) given by

$$F_\phi^{(\rm thin-shell)}/F_{\rm N} = \frac{\lambda_{\rm in}\lambda_{\rm out} - \lambda_{\rm in}^2}{r^2} \tag{20}$$

gives qualitatively reasonable results.

In Fig. 1, we compare the two solutions, where the solid lines in the top panel show the numerical solutions for the ratio of forces η as a function of the two dimensionless parameters $r/\lambda_{\rm out}$ and $\lambda_{\rm out}/\lambda_{\rm in}$,

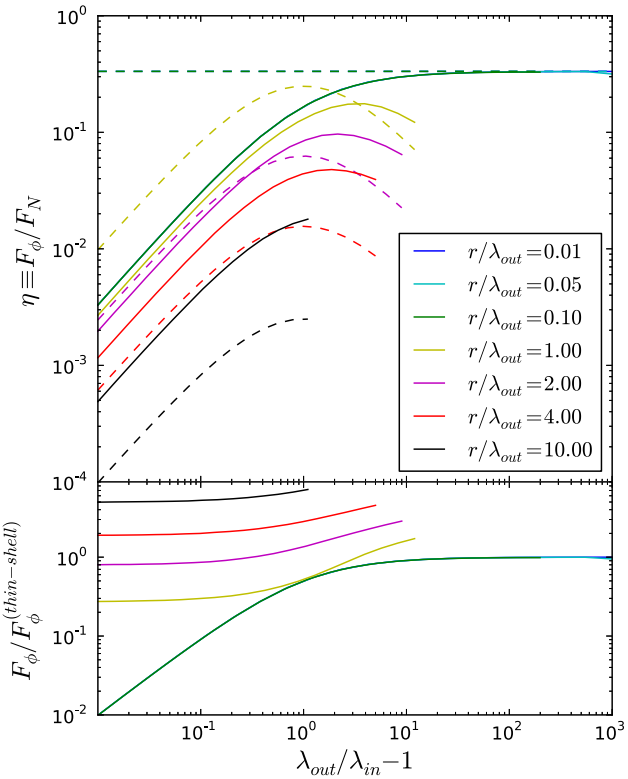

Figure 1. Top panel: we compare the value of the force ratio $\eta = F_\phi/F_{\rm N}$ in both the exact solution (solid lines) and the thin-shell approximation (dotted lines). For $r/\lambda_{\rm out} > 10$ the fifth force is less than 2 per cent of the strength of gravity. Thus we do not need the exact solution and can approximate the fifth force as zero there. Bottom panel: the ratio of the curves in the top panel. The approximate solution is accurate for small $r/\lambda_{\rm out}$, large $\lambda_{\rm out}/\lambda_{\rm in}$ values, but otherwise does not reproduce well the exact result. At small $\lambda_{\rm out}/\lambda_{\rm in}$ however, the fifth force is quite weak anyway, so we can set it to zero safely.

while the dotted lines show the thin-shell approximation. $\lambda_{\rm out} > \lambda_{\rm in}$ means that the density inside the top-hat region is greater than outside, which is the case for haloes. Both solutions are qualitatively the same:

(i) When the exterior and interior Compton wavelengths are very close in magnitude, the fifth force is negligible compared to gravity, because the scalar field takes very similar values inside and outside the overdensity, making its gradient (i.e. the fifth force) small.

(ii) As $\lambda_{\rm out}$ increases, the fifth force grows in importance until $\lambda_{\rm out} \sim$ a few $\times\ \lambda_{\rm in}$, after which the ratio $\eta = F_\phi/F_{\rm N}$ decreases. This can be understood as follows: suppose $\lambda_{\rm in}$ remains unchanged, then an increase in $\lambda_{\rm out}$ with fixed $r/\lambda_{\rm out}$ means that the radius of the overdensity, and so the Newtonian potential $\Phi_{\rm N} \propto r^2 \propto \lambda_{\rm out}^2$, is increased; meanwhile, according to the thin-shell approximation, the fifth-force-to-gravity ratio is proportional to $|\phi_{\rm out} - \phi_{\rm in}|/\Phi_{\rm N}$, with $\phi_{\rm out} \approx \alpha\rho_\Lambda/\gamma\rho_{\rm out} \propto \lambda_{\rm out}$ for our model: when $\phi_{\rm out}$ is close to $\phi_{\rm in}$, i.e. when $\lambda_{\rm out}/\lambda_{\rm in} \sim 1$, $|\phi_{\rm out} - \phi_{\rm in}|$ increases faster than $\Phi_{\rm N}$, making η increase; but when with $\phi_{\rm out} \gg \phi_{\rm in}$, η becomes $\propto |\phi_{\rm out}/\Phi_{\rm N}| \propto \lambda_{\rm out}^{-1}$, which decreases with $\lambda_{\rm out}$. Physically, there are two parts of the screening, self and environment screening: the self-screening becomes stronger with increasing mass (and therefore increasing r), while the environment screening becomes weaker with decreasing environmental density (and therefore increasing $\lambda_{\rm out}$). The behaviour of η, with $r/\lambda_{\rm out}$ fixed, is the result of the competition of the two.

(iii) The fifth force ratio η decreases monotonically with increasing radius r of the spherical overdensity, for fixed $\lambda_{\rm out}$. This is because a larger r means that the overdensity is more massive, and therefore more efficient self-screening of the fifth force in given environment (specified by $\lambda_{\rm out}$).

Note that for the $r/\lambda_{\rm out} = 0.01$, 0.05 and 0.1 cases, the dashed lines are all horizontal and all overlap each other. Likewise, for those cases the solid lines all overlap each other.

Next we explore in more detail the differences between the thin-shell formula and our exact numerical solution, showing that the thin-shell formula has the expected deviation in various regimes. The differential equation that gives Fig. 1 is equation (17), which has a step function as its source on the right-hand side. For the sake of discussion, we can fix this step function by fixing the value of $\lambda_{\rm out}/\lambda_{\rm in}$, which means that we are looking at a fixed horizontal coordinate in Fig. 1. Let us also assume that $\lambda_{\rm out}/\lambda_{\rm in}$ is small. We are interested in the solution to $\mathrm{d}\psi/\mathrm{d}\tau$ which governs η according to equation (19). Remember that we are interested in forces at the edge of the spherical top hat, i.e. where the step function jumps so that $\tau = r/\lambda_{\rm out}$.

Consider the cases where $r/\lambda_{\rm out}$ is large, and assume further that we fix $\lambda_{\rm out}$ but keep increasing r. Because r is very large, the scalar field will settle to $\phi_{\rm in}$ at some point when we move from outside the top hat to inside the top hat, before we reach the centre of the body. As a result, as long as r is much larger than $\lambda_{\rm out}$, the transition of the scalar field from $\phi_{\rm out}$ to $\phi_{\rm in}$ will get insensitive to the exact value of r. The fifth force at the edge of the top hat will therefore be insensitive to the exact value of r also.

The upper panel of Fig. 1 shows the fifth-force-to-gravity ratio. For very large r, the fifth force is insensitive to r as argued above, while standard gravity is proportional to r. As a result, moving from the black solid line to the red solid line (r is decreased by a factor 2.5) there should be an increase of the same factor in η, which is indeed the case. The thin-shell approximation, on the other hand, predicts that η is proportional to $1/r^2$. This is given in equation (20). Therefore, moving from the black dashed line to the red dashed line there is an increase by a factor of $2.5^2 = 6.25$. We can therefore see why the thin-shell condition predicts a more sensitive dependence on r than the exact solution, and why the various dashed curves differ more than the solid curves.

This calculation shows that the thin-shell condition is actually quite poor in some situations. The problem of this approximation is the following: it assumes that all matter inside the thin shell contributes to the fifth force in the same way as it contributes to the standard gravity, while in reality it is only the gradient of the scalar field at the edge of the spherical top hat that matters. The two can be quite different.

On the other hand, when r is small, we are in the linear perturbation regime and the fifth force should depend on r in the same way as the standard gravity, which is why η becomes insensitive to r. This explains the overlapping of the blue, cyan and green curves in Fig. 1. However, for small values of $\lambda_{\rm out}/\lambda_{\rm in}$, the numerical solution predicts $\eta \ll 1$ instead of $\eta = 1/3$ as given by the thin-shell condition. The cause of this failure of the thin-shell solution is as follows. As the densities inside and outside the top hat approach each other, the scalar field becomes homogeneous and the fifth force, which is the gradient of the scalar field, goes to zero. Meanwhile, the standard gravity is calculated using the mass within the top hat, and will always be a constant if r and $\rho_{\rm in}$ do not change. So their ratio should be smaller and smaller in order to make $\rho_{\rm out}$ closer and closer to $\rho_{\rm in}$.

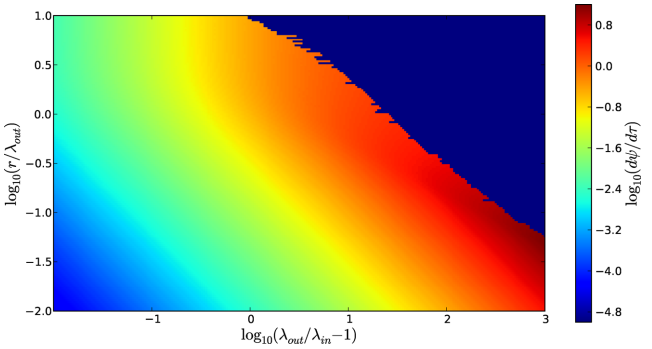

Figure 2. The solution of equation (17) as a function of dimensionless parameters $r/\lambda_{\rm out}$ and $\lambda_{\rm out}/\lambda_{\rm in}$, in the overdensity case for which $\lambda_{\rm out}/\lambda_{\rm in} > 1$. The fifth force $F_\phi \propto \mathrm{d}\psi/\mathrm{d}\tau$ grows monotonically with either quantity, for all relevant parameter space. The top-right corner is numerically difficult to solve, but we have verified that this regime of parameter space is not used in obtaining the Eulerian barriers.

To summarize, while it is usually qualitatively accurate, the thin-shell solution can be up to a factor of 10 too large or too small. The thin-shell solution is quantitatively correct only in the regime in which the exterior Compton wavelength is much larger than both the overdensity radius and its interior Compton wavelength. This is where the fifth force has its largest magnitude relative to gravity, $F_\phi = F_{\rm N}/3$, the thick-shell regime, and for other regimes we need to go beyond the thin-shell approximation to be accurate. Because the Eulerian environment results of this work require the fifth force solution for both over and underdensities (and because the thin-shell approximation fails for the latter), we need the exact (numerical) solution in both cases for the sake of continuity and consistency.

3.3 Validation of numerical solution

Having demonstrated that a numerical solution of the fifth force is necessary for both under and overdensities, we proceed to the non-trivial validation of such solutions. The void solutions of equation (17) correspond to the parameter space with $\lambda_{\rm out}/\lambda_{\rm in} < 1$. These are shown in Clampitt et al. (2013) and are numerically straightforward. However, for the overdense case ($\lambda_{\rm out}/\lambda_{\rm in} > 1$), much of the parameter space is difficult to solve. In Fig. 2, we show these solutions of equation (17) as a function of the two dimensionless parameters. In the top-right corner of this plot, we were unable to obtain numerical solutions, and therefore set $\mathrm{d}\psi/\mathrm{d}\tau = 0$ for display purposes. However, according to Fig. 1, the fifth force can still be a significant fraction of gravity in this regime (more precisely, it can have a strength >2 per cent of gravity).

Fortuitously, overdensities with the range of Eulerian radii in which we are interested ($R_{\rm eul} \geq 5\,{\rm Mpc}\,h^{-1}$) do not stray into this unsolved regime. The solutions of Section 4 require calculating the evolution of an overdensity from deep in the matter-dominated era to the present day. Early in cosmic history the $r/\lambda_{\rm out}$ parameter is very large (because both r is large and $\lambda_{\rm out}$ is quite small due to the high density) and $\lambda_{\rm out}/\lambda_{\rm in}$ is only slightly larger than one. Then, for collapsing overdense regions $\lambda_{\rm out}/\lambda_{\rm in}$ grows monotonically with time, while $r/\lambda_{\rm out}$ decreases monotonically with time. Qualitatively, then, all solutions track from the top left of Fig. 2 force table to the bottom right as time passes.

The difficulty of obtaining fifth force solutions is greater for larger objects, corresponding to larger smoothing radii in the initial Lagrangian density field or equivalently smaller s. (Here, $s = \sigma^2$ is the variance of the smoothed linear matter power spectrum, to be

defined below.) However, we have verified that we can obtain the Eulerian barriers (again to be defined below) all the way to a small value of s, that is, down to some $s_{\rm min}$ such that

$$\delta_{\rm lin} > 5\sqrt{s_{\rm min}} = 5\sigma \,. \tag{21}$$

We do not need the barrier solution at such small s since they are seldom hit by random walks starting at the origin. In summary, we have verified that for each timestep with $F_\phi \geq 0.02F_{\rm N}$, we solve the exact numerical solution. For timesteps with $F_\phi < 0.02F_{\rm N}$, we set the fifth force to zero.

4 EVOLUTION OF DENSITY PERTURBATIONS

In our simplified modelling of the evolution of spherical over and underdensities, we make the assumption that the profile remains as a top hat or bucket during the whole course and there are no shell crossings. Under this premise, we need to track the evolution of two shells: the halo (for overdensity cases) or the void (for underdensity cases) shell, with proper radius $r_{\rm in}(t)$, as well as the shell of the environment that co-evolves with the over or underdensity inside it (Li & Efstathiou 2012), with radius $r_{\rm env}(t)$. The evolution equation is given by

$$\frac{\ddot{r}_j}{r_j} = -\frac{1}{6M_{\rm Pl}^2}\left[\rho_j(1+\eta) - 2\rho_\Lambda\right], \tag{22}$$

where $\rho_j \equiv 3M_j/4\pi\, r_j^3$ is the matter density in the spherical shell and the constant $\rho_\Lambda \approx V(\phi)$ is the effective dark energy density defined in Section 3.1. The notation r_j denotes $r_{\rm in}$ or $r_{\rm env}$.

The only difference between the evolution of the inner shell and that of its environment is the effect of the fifth force. For the inner shell we calculate the fifth force, whereas the larger environment shell is approximated as evolving under general relativity (GR), $\eta = 0$, because the environment is generally taken to be larger than the Compton wavelength of the scalar field, for which the fifth-force-to-gravity ratio is small (cf. Fig. 1). To calculate the fifth force on the inner shell at each timestep, we use a spherical top-hat profile,

$$\rho(\chi) = \begin{cases} \rho_{\rm in} & \text{for} \quad \chi \leq r_{\rm in} \\ \rho_{\rm env} & \text{for} \quad \chi > r_{\rm in} \end{cases} . \tag{23}$$

The fifth-force-to-gravity ratio is then, using equation (19),

$$\eta = \frac{\sqrt{3\alpha\Omega_\Lambda}\,\gamma\,\frac{{\rm d}\psi}{{\rm d}\tau}\Big|_{\tau=r/\lambda_{\rm env}}}{\frac{1}{2}\Omega_{\rm m}\,(H_0R)\,(ay_{\rm in})^{-2}} , \tag{24}$$

for the inner shell. Following the general excursion set literature, in Li & Efstathiou (2012) and Clampitt et al. (2013), equation (22) is recast to a simpler form by making several changes of variable: they define $N \equiv \ln(a)$ and $y_j(t) \equiv r_j(t)/a(t)R_j$, where R_j is the initial comoving radius. Derivatives with respect to N are denoted by $y' = {\rm d}y/{\rm d}N$. We do not repeat in detail here, but only show the result from those references:

$$y_j'' + \left[2 - \frac{3}{2}\Omega_{\rm m}(N)\right] y_j' + \frac{\Omega_{\rm m}(N)}{2}\left[y_j^{-3}(1+\eta) - 1\right] y_j = 0 \,, \tag{25}$$

with initial conditions specified at $a_{\rm ini} \ll 1$ (deep into the matter-dominated epoch), as

$$y_j(a_{\rm ini}) = 1 - \delta_{j,{\rm ini}}/3, \quad y_j'(a_{\rm ini}) = -\delta_{j,{\rm ini}}/3 \,. \tag{26}$$

Note that in the above, $\Omega_{\rm m}(N) \equiv \Omega_{\rm m}{\rm e}^{-3N}/(\Omega_{\rm m}{\rm e}^{-3N} + \Omega_\Lambda)$, and $\Omega_\Lambda(N) \equiv \Omega_\Lambda/(\Omega_{\rm m}{\rm e}^{-3N} + \Omega_\Lambda)$. $\delta_{j,\,{\rm ini}}$ is the initial density perturbation of the spherical patch ($j = {\rm in}$) or its environment ($j = {\rm env}$).

Thus, the solution is given by considering two second-order differential equations, equation (25) with $j = [{\rm in}, {\rm env}]$ along with the boundary conditions given in equation (26). The force ratio η in equation (24) at arbitrary time is obtained by interpolating the table (cf. Fig. 2) for both haloes (overdensities, cf. Fig. 2) and voids (underdensities), which is straightforward provided the values of $r/\lambda_{\rm out}$ and $\lambda_{\rm out}/\lambda_{\rm in}$ at that time.

5 VOID ASSIGNMENT IN THE EXCURSION SET: LAGRANGIAN VERSUS EULERIAN

In this section, we first briefly review some of the key aspects of a recently proposed void-assignment formalism based on Eulerian arguments (in contrast to the traditional Lagrangian-based approach). We will then describe how to extend this Eulerian-based void assignment to modified gravity theories. For clarity, we will choose a single set of parameters $(\alpha, 2\gamma^2) = (10^{-6}, 1/3)$ to demonstrate the formalism, and in a future work we plan to apply the methodology developed in this work to study void abundances in a class of chameleon-like theories.

5.1 Void assignment in excursion set formalism

The excursion set formalism (Bond et al. 1991) was initially applied to describe the abundance of haloes: the calculation is mapped to the computation of the first crossing distribution across some prescribed barriers (see for example, Zentner 2007, for a review). In its simplest form, the first crossing across a constant barrier whose amplitude is obtained from the spherical collapse model is evaluated for random walks whose heights depend on the linearly extrapolated matter power spectrum as well as the smoothing window filter: analytic solutions are available for sharp-k filter (Zhang & Hui 2006; Lam & Sheth 2009). Recent developments improve the model by including scale-dependent (Sheth & Tormen 1999, 2002) barriers, diffusive barriers (Maggiore & Riotto 2010b; Corasaniti & Achitouv 2011), random walks with correlated steps (Maggiore & Riotto 2010a; Musso & Sheth 2012; Paranjape, Lam & Sheth 2012a), and peak constraints (Paranjape & Sheth 2012; Paranjape, Sheth & Desjacques 2013).

The formation of voids, the biggest underdense regions in the Universe, can also be formulated in the excursion set formalism. Sheth & van de Weygaert (2004) demonstrated that this calculation has to include an additional criterion in order to avoid overcounting the number of voids: the so-called void-in-cloud effect in which voids sitting in overdense regions where haloes are forming should be excluded. Technically, this is realized in the excursion set formalism by imposing two barriers for halo (denoted by $\delta_{\rm c}$) and void (denoted by $\delta_{\rm v}$) formation, respectively. One then computes the first down-crossing probability across the void formation barrier of random walks that *never* crossed the halo formation barrier at larger smoothing scales. Sheth & van de Weygaert (2004) provided an analytical solution for the case where both halo and void barriers are constant; Lam, Sheth & Desjacques (2009) generalized the solution to barriers of arbitrary shapes. Some more recent attempts of formulating void abundance include Eulerian void assignment (Paranjape et al. 2012b, more details below), modifying the mapping from Lagrangian volume to abundance (Jennings, Li & Hu 2013), and introducing diffusive barriers (Achitouv, Neyrinck & Paranjape 2013). In this work, we will focus on extending the Eulerian void assignment in a context in which gravity is modified.

The main purpose of the Eulerian void assignment is to look for the biggest Eulerian volume that satisfies the void criteria:

having a density below 20 per cent of the background. Conservation of mass requires the Lagrangian patch to expand five times (in volume). Another essential assumption in the formalism is no shell crossing: while the relative separations change, concentric shells (and hence the mass within them) preserve their orderings (see for example, Sheth 1998, for discussion). Hence, the immediate environment would have significant impact on the formation of voids: the void in cloud described above is a special case in which the surrounding environment collapses into a vanishing Eulerian size. (Note that it is only a limiting case in which the spherical collapse approximation results in vanishing volume. In reality haloes are virialized objects with physical sizes.) However, this is only part of the picture: halo forming is not a necessary condition to modify the formation of voids. For example, if an underdense region is embedded in a slightly overdense environment, the comoving volume of this slightly overdense environment would decrease and restrict the expansion of the underdense patch. Whether a void would be formed depends on the *Eulerian* size of the surrounding overdensity environment. There are three possibilities:

(i) A void of the same size as predicted by the Lagrangian treatment (Sheth & van de Weygaert 2004) will be formed.
(ii) A void will be formed; however, its size is smaller than its Lagrangian treatment counterpart.
(iii) No void will be formed (in other words the limiting case where the void size is zero).

As a result, the Eulerian-volume void assignment consists of a remapping of the size of the void being formed and the volume function of voids is modified accordingly. For clarity, we refer to this Eulerian void assignment as the PLS (Paranjape et al. 2012b) void assignment in the following.

The evolution of the Eulerian volume of the surrounding environment is a key ingredient in the PLS void assignment. In Paranjape et al. (2012b), they use the following spherical collapse approximations (Bernardeau 1994; Sheth 1998):

$$\Delta_{\rm NL} \equiv \frac{M}{\bar{\rho} V_{\rm E}} \approx \left(1 - \frac{\delta_{\rm l}}{\delta_{\rm c}}\right)^{-\delta_{\rm c}} \tag{27}$$

to obtain the relationship between the Lagrangian volume (equivalently, the total enclosed mass M) and the linearly extrapolated density contrast ($B_{V_{\rm E}} = \delta_{\rm l}$) for a given Eulerian volume $V_{\rm E}$:

$$B_{V_{\rm E}}(M) = \delta_{\rm c}\left[1 - \left(\frac{M}{\bar{\rho} V_{\rm E}}\right)^{-1/\delta_{\rm c}}\right]. \tag{28}$$

$B_{V_{\rm E}}(M)$ defines a barrier in the $\delta_{\rm l}$–s plane for Eulerian volume $V_{\rm E}$, where S is the variance of the smoothed linear power spectrum over a Lagrangian volume $V_{\rm L}$ which satisfies $M = \bar{\rho} V_{\rm L}$,

$$s \equiv \sigma^2(M) = \int \frac{{\rm d}^3 k}{(2\pi)^3} P(k) W^2(k R_{\rm L}), \tag{29}$$

in which $W(kR_{\rm L})$ is the Fourier transform of the smoothing window function and $R_{\rm L}$ is the Lagrangian radius associated with the Lagrangian volume $V_{\rm L}$.

Note that equation (28) defines a monotonically decreasing barrier in the $\delta_{\rm l}$–s plane and its limiting value for $\Delta_{\rm NL} \to \infty$ is $\delta_{\rm c}$. When $\Delta_{\rm NL} = 0.2$ and $\delta_{\rm c} = 1.676$, $B_{V_{\rm E}, \Delta_{\rm NL}=0.2}(M) \approx -2.76$ which is the constant void formation barrier. Sheth (1998) and Lam & Sheth (2008a) discussed the application of the excursion set with barrier defined in equation (28) to obtain the mass distribution at some fixed Eulerian volume.

Changing $V_{\rm E}$ in equation (28) results in a series of nested curves whose heights are lower for increasing $V_{\rm E}$. The limiting case where

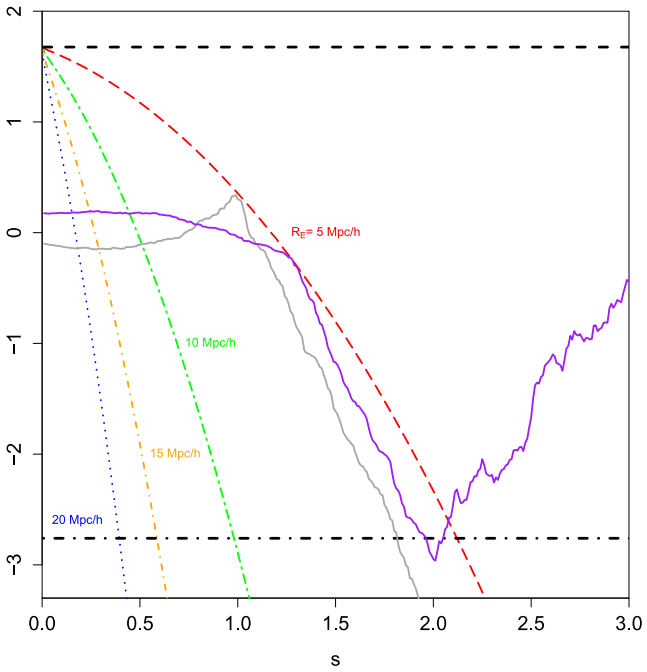

Figure 3. Illustration of Eulerian void assignment. Barriers for four different Eulerian volumes are shown, together with the constant barriers for halo (top thick dashed) and void (bottom thick dot–dashed) formation. Two sample random walks shown demonstrate the characteristics of Eulerian versus Lagrangian void assignment (see text for descriptions).

$V_{\rm E} \to 0$ is a constant barrier $B_{V_{\rm E}} = \delta_{\rm c}$ and this corresponds to the halo formation barrier. The PLS algorithm looks for the biggest Eulerian volume which has a density contrast of -0.8: we are looking for random walks that cross some Eulerian barriers below the threshold $\delta_{\rm v} = -2.76$. For each random walk, we start from a very large Eulerian volume. Since the Eulerian barrier associated with a big volume is decreasing very rapidly, the random walk almost always pierce that barrier above $\delta_{\rm v}$. As we gradually decrease the Eulerian volume, the flattening of the barrier allows the random walk fluctuates before piercing the barrier. Ultimately, one may find an Eulerian volume whose barrier is only pierced by the random walk below $\delta_{\rm v}$ and this Eulerian volume is the Eulerian size of the void associated with the random walk. Fig. 3 uses two sample random walks to illustrate the characteristic of PLS void assignment (note: these walks are for demonstration purposes and while non-vanishing heights at $s = 0$ are unphysical, they do not affect our discussion). Two thick horizontal curves are halo (top) and void (bottom) thresholds in GR. Four decreasing barriers show Eulerian barriers for different Eulerian sizes. Both walks represent void-forming regions in Lagrangian void assignment: they cross the bottom barrier (at approximately $s = 1.8$ and 2, respectively) without crossing the upper constant barrier at smaller s, and as such they represent voids of similar sizes in the Lagrangian-void-assignment scheme. The result is very different when Eulerian void assignment is considered: the grey walk is going to form a void of Eulerian radius of 5 Mpc h^{-1} while the purple walk is not a void (in the regions shown). The red decreasing barrier corresponds to an Eulerian size $R_{\rm E} = 5$ Mpc h^{-1}. The grey walk touches it at around $s = 1$ but the walk never pierces this barrier above $\delta_{\rm v}$. To see it is the biggest Eulerian size allowed for the grey random walk, imagine we increase the Eulerian size by $\Delta R_{\rm E}$. The Eulerian barrier associated with $R_{\rm E} + \Delta R_{\rm E}$ lies somewhere between the green and red

barriers – the grey random walk will pierce such barrier with $\delta_l > \delta_v$, and as a result the density contrast within $R_E + \Delta R_E$ will be higher than 20 per cent of the background. This sudden increase in mass corresponds to the wall around the void as discussed in Paranjape et al. (2012b).

The purple random walk has a different story: although it crosses the δ_v barrier without crossing the δ_c barrier, the random walk pierces the red Eulerian barrier at around $s = 2.1$, above the δ_v barrier. For this particular walk, one would need to consider smaller Eulerian sizes (and hence the barrier will be shallower) to check if a void would be formed (not shown here).

We would like to point out two important characteristics of this PLS void assignment as compared to the Lagrangian version.

(i) Random walks identified as void forming in Lagrangian void assignment (crossing δ_v at some S but never crossed δ_c for $s < S$) may not form a void. However, the reverse is true: PLS assigned voids are always associated with a Lagrangian counterpart.

(ii) PLS assigned voids cannot be bigger than the corresponding Lagrangian-assigned voids.

5.2 Void assignment in modified gravity models

The above discussion on Eulerian void assignment applies to models where the gravity is described by GR. In this section, we describe how to extend the various void assignments to modified gravity models. Clampitt et al. (2013) discussed the extension of Lagrangian void assignment and found that the abundance of voids would constrain modified gravity models. In particular, the signature of MG is stronger at the bigger voids, which also justifies their approximation of neglecting the void-in-cloud effect. In what follows we review how to apply the Lagrangian void assignment in modified gravity models as well as describe how to apply the PLS void assignment.

In models with MG, the dynamics is modified by the presence of the fifth force, whose strength can depend on the environmental density. Thus, all the barriers involved are modified accordingly. There are multiple scales involved in this case: an environmental scale corresponding to halo formation, as well as various Eulerian volumes and their corresponding environments against which the void formation criteria are checked. As discussed in Li & Efstathiou (2012), the environment should be big enough to encompass the objects being considered, but at the same time give a representative environment to that particular object (hence it cannot be too large). Li & Lam (2012) and Lam & Li (2012) proposed using an Eulerian size of $R_h = 5$ Mpc h^{-1} (which was roughly the Compton wavelength of the scalar filed in the models considered) as the environment for halo formation and we will adopt the same here. For void formation, Clampitt et al. (2013) suggested a scale five times the void radius as the environment, each we also adopt here. While Lagrangian environment is used in Clampitt et al. (2013), we use Eulerian environment in the following since it allows us to follow the evolution of the Eulerian volumes closely. Notice that previous studies always assume the evolution of the environment follows that of GR since it is always much bigger than the Compton wavelength of the scalar field being considered. We will also make this assumption in the following discussion.

We apply the PLS void assignment as follows. We first generate the following tables of different barriers for different environmental densities δ_{env} (here δ_{env} is the linear density contrast of the environment, extrapolated to today using the ΛCDM linear growth factor; $\delta_{env} > 0$ denotes overdense environments and vice versa):

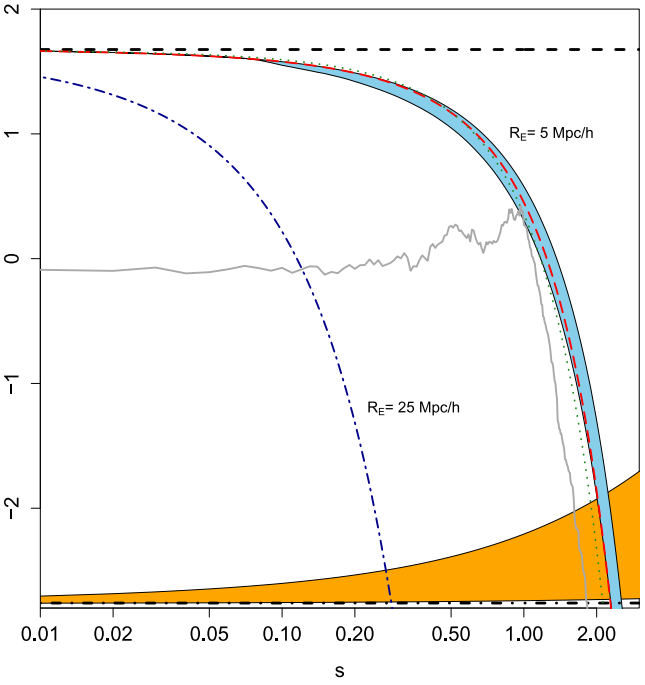

Figure 4. Illustration of the PLS void assignment in modified gravity models (see text for description). The constant barriers at the top and the bottom are the halo and void formation threshold, respectively, in GR. The orange-shaded region is the void formation barriers in modified gravity model for $-2.4 \leq \delta_{env} \leq 1.5$. Eulerian barriers for $R_E = 5$ Mpc h^{-1} are shown: the red curve going through the blue-shaded region is the corresponding GR barrier while the blue-shaded region shows the MG barriers with the same range of δ_{env} as in the void formation. The green dotted curve shows the spherical collapse approximation (equation 28) in GR.

(i) halo formation barrier (in GR it is a constant barrier at δ_c);

(ii) void formation barrier (in GR it is again a constant barrier at δ_v);

(iii) Eulerian barriers $B_V(S|\delta_{env})$ for each Eulerian volume V_E.

Although we assume that the evolution of all the environments would be described by GR, we use the same numeric solver to obtain the GR Eulerian-volume barrier for consistency. Fig. 4 shows results for different barriers. For an Eulerian size of 5 Mpc h^{-1}, the blue-shaded region corresponds to its Eulerian barriers for a wide range of environmental density contrast ($-2.4 \leq \delta_{env} \leq 1.5$). The red dashed curve running from the top of the shaded region at small s to the bottom of the shaded region at big s is the GR Eulerian barrier computed by the same numerical solver. On the other hand, the green dotted curve shows the approximation formula equation (28).

Fig. 5 shows the difference between barriers of three different Eulerian sizes from the GR counterparts. Three environmental density contrasts ($\delta_{env} = -2.4$, 1.5, 0) are chosen for comparison, and the result shows the following features.

(i) At very large scales (small s), there is no difference between the GR and MG barriers. At larger s, the two deviate from each other: the deviation starts at smaller s for bigger Eulerian size since, with δ_{env} fixed, to have a bigger Eulerian size the initial density δ_l is in general lower (cf. Fig. 4), which means the effect of the fifth force is stronger.

(ii) Whether the Eulerian barriers in MG are higher or lower than their GR counterparts depends on the relative density

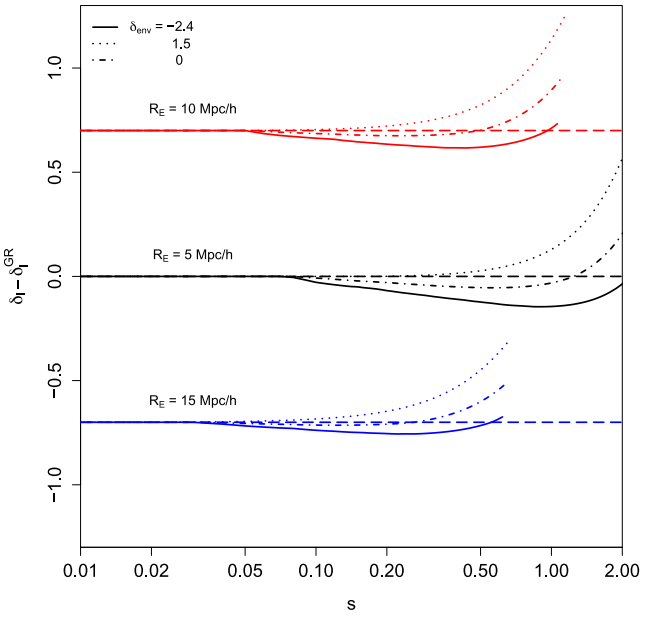

Figure 5. Difference between the MG and GR Eulerian barriers for $R_E = 5$, 10, 15 Mpc h^{-1} for three different environmental overdensities. The results for $R_E = 10$ and 15 Mpc h^{-1} are shifted by ± 0.7. We truncate the comparison for $\delta_l < -3$.

contrast to the environment. If the density inside is higher than that in the environment, the fifth force is attractive (i.e. points towards the centre) and slows down the expansion. To have the same R_E today, the patch needs to have a lower initial density that helps to speed up the expansion. If the density inside is lower than that in the environment, the fifth force helps the expansion, which has to be compensated by having higher initial densities in the patch. A special case is when $\delta_l = \delta_{env}$, so that the fifth force vanishes identically throughout the evolution: here $\delta_l = \delta_l^{GR}$, and is where the curves cross zero in Fig. 5. As an example, take the dotted curves in Fig. 5, which correspond to a very dense environment ($\delta_{env} = 1.5$) so that the barrier is higher in MG for most values of s; however, when s is extremely small, the initial size of the patch is huge and for it to evolve to a given R_E today its initial density has to be higher than 1.5, so that the patch must be overdense. In this case, the MG barrier becomes lower than in GR. This trend is followed by all curves in Fig. 5, which only differ by their values of s at which $\delta_l - \delta_l^{GR}$ crosses zero.

To better understand the physics, we shall build up the PLS-void-assignment scheme step by step, following three steps.

5.2.1 *Void barrier (1 barrier)*

As discussed in Clampitt et al. (2013), we fix the environment to be five times the size of the resulting voids. The void formation critical density depends on the environmental density at the corresponding environment. The first crossing distribution is therefore

$$f(S) = \int_0^S \mathrm{d}s\ f(\delta_{env}, s; R_{env}) f(S, \delta_v(\delta_{env})|s, \delta_{env}), \qquad (30)$$

in which $f(\delta_{env}, s; R_{env})$ is the first crossing probability of the environmental barrier of Eulerian size R_{env} that corresponds to a void of size S – it is five times the void size. $f(S, \delta_v(\delta_{env})|s, \delta_{env})$ is the conditional first crossing probability of the modified void formation criteria density, after having first crossed the environment Eulerian barrier at (s, δ_{env}). Notice that one does not impose the restriction of not crossing the halo formation barrier here.

5.2.2 *Void in cloud (2 barriers)*

The void-in-cloud effect is straightforward to implement: the first crossing across an Eulerian barrier corresponding to a halo formation environment of $R_h = 5$ Mpc h^{-1} is obtained. The resulting δ_{env}^{halo} will be used to compute the halo formation barrier. We then check that the random walks never cross this halo formation barrier to enforce the void-in-cloud condition.

5.2.3 *PLS void assignment*

The implementation of the Eulerian void requires more attention and we will illustrate the idea with the following example. For simplicity assume that we choose a random walk that has not crossed the halo formation barrier. At scale s the random walk has a height δ_l: we would like to get the Eulerian volume V_E at *this point*, and at the moment we neglect previous steps of this walk. In the case of GR, given M and B, one can find the associated Eulerian volume either by looking up the table or by inverting equation (28). In the case of modified gravity models, the exact Eulerian volume V_E associated with (s, δ_l) depends on the environmental density, while the size (and density) of the environment depends on V_E, because we have defined void environment to have five times the size of the void that forms inside it. We use the following iterative process to break this inter-dependence and obtain V_E.

(i) Take a guess for the Eulerian size R_E (for example using the corresponding GR value).
(ii) We now fix the parameters s, δ_l and R_E and vary δ_{env}.
(iii) Set $R_{env} = 5R_E$ and use the GR numerical table to construct the associated environmental barrier (recall that we assume GR applies in the environment).
(iv) The first crossing of the environmental barrier associated with R_{env} gives δ_{env}.
(v) We now fix three parameters: s, δ_l and δ_{env}, and vary R_E.
(vi) We then search the table of Eulerian barriers in modified gravity models, $B_{V_E}(S|\delta_{env})$, for an Eulerian volume V_E' that satisfies the three parameters. This gives a new estimate of R_E'.
(vii) Repeat step (iii) until we finally arrive at a consistent set of $\{s, \delta_l, R_E, \delta_{env}\}$. This is deemed to be achieved when R_E changes by less than 1 per cent, or less than 0.5 Mpc h^{-1} in absolute value, between two consecutive trials, and we call this the convergence of R_E.

The resulting environmental density contrast δ_{env} is then used to obtain the associated MG void formation barrier. This iterative process is applied at each step of the random walk. We then look for the biggest Eulerian volume that the random walk crossed below the corresponding void formation barrier.

Fig. 4 uses a sample random walk to illustrate the idea. We will take the value $s \approx 1$ where the random walk touches the red dashed curve as a demonstration. At this particular value of s, the random walk has a height of around $\delta_l = 0.3$. We now need to find the corresponding Eulerian size for *this* particular value of (s, δ_l). In the case of GR, this Eulerian size would be 5 Mpc h^{-1}. Using this initial guess, we obtain an environmental size of $R_{env} = 25$ Mpc h^{-1}, whose (GR) Eulerian barrier is shown by the blue dot-dashed curve. The first crossing of this environment barrier is approximately $\delta_{env} = -0.1$. We then use this δ_{env} value to find a new R_E' whose

Eulerian barrier will have the value $(s, \delta_{\rm l})$. In this particular case, the Eulerian barrier for $(R_{\rm E}, \delta_{\rm env}) = (5\,{\rm Mpc}\,h^{-1}, -0.1)$ lies somewhere in the blue-shaded region and hence the new $R'_{\rm E}$ value will be slightly larger than 5 Mpc h^{-1}. One then repeat the above procedure until $R_{\rm E}$ converges. This iterative process only gives *one* Eulerian size at any particular point in the random walk. To find the largest Eulerian size that would form a void, one needs to examine the whole random walk – which means that the iteration is done at each step of the walk, with a frequency $\Delta s = 0.0025$ for our numerical implementation.

Notice that the implementation of PLS void assignment is computationally very intensive in the case of modified gravity models. For this reason, we restrict our algorithm to search only for voids having size bigger than 5 Mpc h^{-1} but smaller than 100 Mpc h^{-1}. We believe this range is appropriate since smaller voids are difficult to identify and previous study suggests that the signature of MG lies in the bigger voids. On the other hand, voids bigger than 100 Mpc h^{-1} are extremely rare and this upper limit should not affect our result.

6 RESULTS

Having outlined our methodology, in this section we present the results of the void abundance in our model of MG. In addition to the PLS-void-assignment scheme we described in the previous section, we also include comparisons with the Lagrangian void assignment. We will discuss void abundance derived from both correlated and uncorrelated steps in the random walks. In order to avoid sample variance when computing void abundance, we apply the different algorithms on the same set of random walks in both the uncorrelated and the correlated cases, which is realized by using the same random k-mode value $\delta(k)$ but different window function $W(kR)$ in

$$\delta(x = 0; R) = \int \frac{{\rm d}^3\boldsymbol{k}}{(2\pi)^3}\delta(k)W(kR), \tag{31}$$

to generate the walks. In the uncorrected case, $W(kR)$ is a top-hat filter in k space – because $\delta(k)$ is a Gaussian random number with different k modes independent of each other, and the k-space top-hat filter does not introduce correlations between them, the values of $\delta(x = 0, R)$ are uncorrelated when changing R; in the correlated case the filter is a top hat in real space. Note that we can apply the three algorithms (1 barrier, 2 barriers and PLS) to correlated and uncorrelated walks, and therefore there are in total six ways to assign voids. We run a total of 40 million random walks to get our results. For the PLS method there are 1476 740 (GR) and 2123 162 (MG) voids, respectively.

Fig. 6 shows the first crossing probability of various void-assignment schemes. The top panel shows different predictions for GR while the middle and the bottom panels show the differences in modified gravity models. The black histograms/symbols/curves are the results with uncorrelated steps while the red are correlated steps. Note that in both cases we use the top-hat window function to relate the variance s and the smoothing scale in Lagrangian space.

In the case of GR, the three different void-assigning schemes have very similar results when correlated steps are used (red symbols), showing our Monte Carlo simulations are consistent with the results in Paranjape et al. (2012b). On the other hand, for the uncorrelated steps, the void abundance in the PLS formalism is significantly lower than the other two. The results for single barrier (filled black squares) and two-barrier (solid curve) are the same, indicating that at these (relatively large) smoothing scales the void-in-cloud effect is insignificant (see below). In other words, in the value range of ν (which can be mapped to the void radius, cf. Fig. 7) of interest to us, the expansion of voids is indeed restricted by their environments – the two-barrier void-assignment scheme, which only removes voids-in-cloud that eventually collapses, is oversimplistic and not accurate.

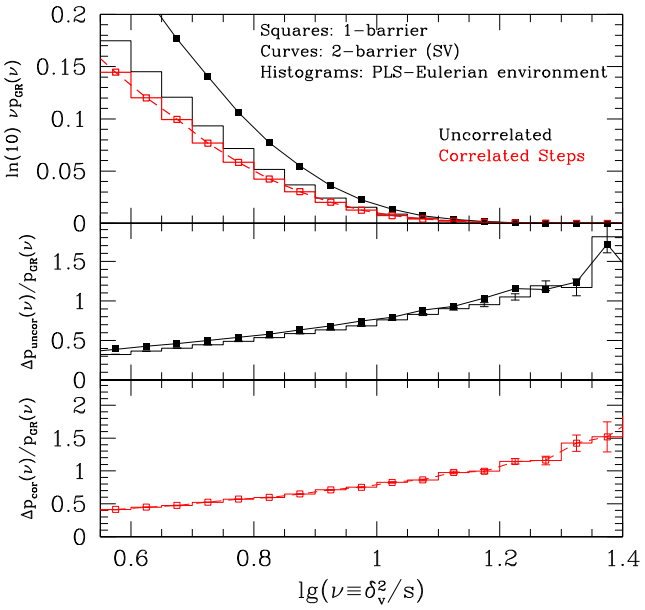

Figure 6. The multiplicity function for various void-assigning schemes in the excursion set approach. The top panel shows various results in GR while the middle and the bottom panels show the relative differences in modified gravity models studied in this paper.

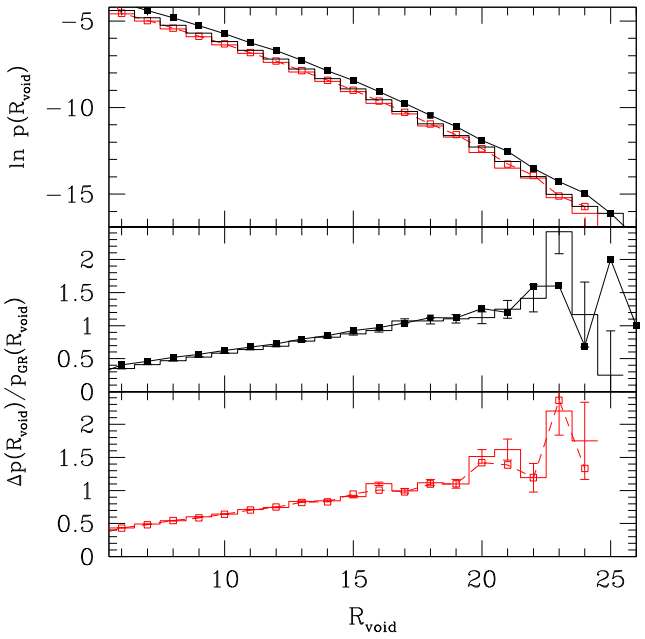

Figure 7. The first crossing probability as a function of the Eulerian void size for various void-assigning schemes in the excursion set approach. Same legends are used as in Fig. 6. The top panel shows various results in GR while the middle and the bottom panels show modifications in modified gravity models with uncorrelated- and correlated-step void-assignment schemes, respectively.

In the middle and the bottom panels, we show the modifications in void abundance in modified gravity models using uncorrelated steps and correlated steps in the random walks, respectively. We only show the error bars of one of the schemes (in both cases the histogram for the PLS method) for clarity. In the middle panel, the filled squares are the modifications for a single void barrier (hence neglecting the void-in-cloud effect) and the solid curve sharing a very similar result shows the modifications in the two-barrier case (including void-in-cloud effect). Since it is very unlikely that these large voids are embedded in even larger patches that are going to form haloes, the results from these two void-assigning methods are nearly the same. Notice that it is not straightforward to directly compare this panel to fig. 6 in Clampitt et al. (2013) since we use Eulerian barrier for the environment as well as a different linear power spectrum generated from CAMB (Lewis 2000) with the recent *Planck* cosmology (Planck Collaboration XVI 2014). None the less the trend in the abundance modification is very similar in both studies. The histogram shows the modifications using the PLS algorithm with uncorrelated steps: for very big voids the results are similar to the other two void algorithms, however there are differences when going to relatively small voids. The modification in void abundance using the PLS algorithm is slightly less than the other algorithms in small voids.

The bottom panel shows the modification of void abundance in modified gravity models for correlated steps. In this case, we employ the top-hat filter in real space and generate a series of random walks. The open squares, the dashed curve and the histogram represent results from the one-barrier, two-barrier and PLS void algorithm, respectively. All of them show very similar results, suggesting that when using correlated steps, one would derive the void abundance using the much simpler one-barrier or two-barrier algorithms. We also checked that while there are some quantitative differences, the results from uncorrelated-step random walk with one-barrier or two-barrier algorithm agree with the more sophisticated correlated steps with PLS algorithm.

In summary, while there are noticeable differences in the void abundances from the different void-assignment schemes, the relative difference between our chameleon model and GR only changes slightly. This is somewhat surprising, but it may simply suggest that void abundance in chameleon models changes with different void assignments in a similar manner as in GR.

Fig. 7 shows the first crossing distribution plotted as a function of the Eulerian sizes of voids being formed. This figure uses the same set of random walks, but since s and R are not linearly related the walks are organized into different bins. We use the same legends as in Fig. 6. One noticeable difference when comparing the middle and the bottom panels with those of Fig. 6 is stronger modifications at very large voids: although very rare, the abundance of large voids (larger than 20 Mpc h^{-1}) is a very sensitive probe of modified gravity models. Notice that the model parameters used in this work are mild such that the fifth force helps to enhance the halo mass function by $\lesssim$15 per cent across the whole mass range at $z = 0$ (Li & Efstathiou 2012); in contrast, for the void radii studied in this work, we can see that the fifth force can enhance the void abundance by over 50 per cent (and over 100 per cent for $R_{\rm void} > 15$ Mpc h^{-1}).

7 SUMMARY AND DISCUSSION

In this paper, we considered the void abundance in the chameleon-type modified gravity models – we have extended previous work in Clampitt et al. (2013) and Paranjape et al. (2012b) to compute the void volume function in modified gravity models, using the recently developed Eulerian-void-assignment (PLS) scheme within the excursion set approach and to compare its result to other void-assignment schemes. This Eulerian void method includes the effect of the surrounding on the growth of void – it would reduce the size of the void or even disqualify it as a void (if the surrounding collapses). A brief description of this PLS void method is included in Section 5.1.

In order to implement this PLS-void-assignment method in modified gravity models, we solved the spherical collapse equation of motion for various environmental density contrasts, to calculate the critical density contrasts for halo and void formation. We performed validation test on the numerical solver to make sure the barriers being used in the excursion set approach are correct. We then applied these barriers to evaluate the first crossing probability using Monte Carlo simulations: we used both correlated- and uncorrelated-step random walks on various void-assigning schemes. Correlated- and uncorrelated-step random walks are associated with the window function kernel used to define the Lagrangian patches: the former corresponds to top-hat or Gaussian window functions while the latter to a sharp-k filter.

We then discussed the implementation of the excursion set approach for void volume function in modified gravity models in Section 5.2. The one-barrier and two-barrier cases are relatively straightforward, while we introduce an iterative method in the PLS formalism to obtain a consistent description of the parameter set $\{s, \delta_1, R_{\rm E}, \delta_{\rm env}\}$ – it is important since the evolution of structure depends on the strength of the fifth force, and hence the environmental density contrast. Notice that these are implemented using the Eulerian picture.

The results of our calculation are summarized in Figs 6 and 7. Our results are consistent with those in Clampitt et al. (2013): the abundances of voids are very sensitive to MG. One unexpected finding is the modifications in the void volume function due to modified gravity models using the one-barrier and two-barrier methods with uncorrelated steps match those using the PLS method with correlated steps very well. We believe this would be a coincidence – the fact that the bases of comparison (i.e. the GR predictions, see the top panel) are very different supports it.[1] On the other hand, the results of the relatively straightforward one-barrier with correlated steps agree with those of the PLS algorithm, for both the GR results as well as the modifications due to modified gravity models. Hence when dealing with correlated steps, it is sufficient to compute the void abundance using the one-barrier method – either with Monte Carlo simulations as we did in this work or with one of the approximations developed for computing first crossing probability.

The enhancement of void abundances due to modified gravity model shows different characteristic than that of halo abundances: the chameleon screening is less efficient for these underdense regions and hence the abundances of voids (in particular large ones) are very sensitive to MG. Furthermore, there is detriment in the abundance of low-mass haloes due to mass conservation while the void abundance is always enhanced (down to the scale we investigate). By combining the abundances of haloes and voids, it is possible to break the degeneracy between modified gravity models and other cosmological parameters or models, such as σ_8 and

[1] Another possibility is that the application of the PLS-void-assignment method with correlated steps introduces the same differences to the simpler 1-barrier or 2-barrier results, and when taking the relative change this gets cancelled out to a large extent.

massive neutrinos, a possibility which merits further investigations in the future.

While void abundance is a sensitive probe of modified gravity models, there are several complications needing to be addressed before it can be used to put constraints on these models. First, real void catalogues are constructed using biased tracers in galaxy surveys, while our study assumes that voids are found from the dark matter field. This may introduce biases – since MG modifies halo abundance (hence galaxies) as well, such biases may be different for GR and modified gravity models. Secondly, the predictions from the excursion set approach do not agree with the void catalogues generated using dark matter particles simulations, even for the ΛCDM paradigm (see for example Achitouv et al. 2013; Jennings et al. 2013). Different methods are proposed to circumvent this discrepancy but it is important to check for consistency in both GR and modified gravity models if any of these methods was used in the comparison analysis. Thirdly, the increase of void abundance in modified gravity models aggravates the problem of having a void volume fraction larger than unity. Notice that the excursion set approach only considers structure formation at each position *independently* – while this may be reasonable for collapsing objects (haloes), objects (voids) having their comoving sizes expanded may have a larger chance to merge with each other, invalidating the assumption of the excursion set approach – this problem will be worse in the presence of the fifth force, which helps inflate the voids faster. Fourthly, given that the fifth force is less efficiently suppressed in voids, the evolution and properties of galaxies there can also be different from in GR, adding more subtlety to the interpretation of observational data and constraints using them.

Finally, as pointed out in Clampitt et al. (2013), since voids sitting in overdense environments show stronger signatures of modified gravity models (at least for the chameleon-type theories), one would possibly increase the signal to noise by using the conditional void volume function, or by constructing a weighted void volume function. The latter method is now being investigated with both weighted halo mass function as well as weighted void volume function.

ACKNOWLEDGEMENTS

JC is partially supported by Department of Energy grant desc0007901. YC is supported by the Durham Junior Research Fellowship. BL is supported by the Royal Astronomical Society and the Department of Physics of Durham University. YC and BL acknowledge a grant with the RCUK reference ST/F001166/1.

REFERENCES

Achitouv I., Neyrinck M., Paranjape A., 2013, preprint (arXiv:1309.3799)
Bernardeau F., 1994, ApJ, 427, 51
Bond J. R., Cole S., Efstathiou G., Kaiser N., 1991, ApJ, 379, 440
Bos E. G. P., van de Weygaert R., Dolag K., Pettorino V., 2012, MNRAS, 426, 440
Cai Y.-C., Li B., Cole S., Frenk C. S., Neyrinck M., 2014a, MNRAS, 439, 2978
Cai Y.-C., Neyrinck M. C., Szapudi I., Cole S., Frenk C. S., 2014b, ApJ, 786, 110
Clampitt J., Jain B., 2014, preprint (arXiv:1404.1834)
Clampitt J., Cai Y.-C., Li B., 2013, MNRAS, 431, 749
Clifton T., Ferreira P. G., Padilla A., Skordis C., 2012, Phys. Rep., 513, 1
Corasaniti P. S., Achitouv I., 2011, Phys. Rev. D, 84, 3009
Davis A. C., Lim E. A., Sakstein J., Shaw D. J., 2012, Phys. Rev. D, 85, 123006
Granett B. R., Neyrinck M. C., Szapudi I., 2008, ApJ, 683, L99
Hamaus N., Wandelt B. D., Sutter P. M., Lavaux G., Warren M. S., 2014, Phys. Rev. Lett., 112, 041304
Hotchkiss S., Nadathur S., Gottlöber S., Iliev I. T., Knebe A., Watson W. A., Yepes G., 2015, MNRAS, 446, 1321
Hoyle F., Vogeley M. S., 2002, ApJ, 566, 641
Hoyle F., Vogeley M. S., Pan D., 2012, MNRAS, 426, 3041
Hu W., Sawicki I., 2007, Phys. Rev. D, 76, 064004
Ilić S., Langer M., Douspis M., 2013, A&A, 556, A51
Jain B., Khoury J., 2010, Ann. Phys., 325, 1479
Jennings E., Li Y., Hu W., 2013, MNRAS, 434, 2167
Khoury J., Weltman A., 2004, Phys. Rev. D, 69, 044026
Lam T. Y., Li B., 2012, MNRAS, 426, 3260
Lam T. Y., Sheth R. K., 2008a, MNRAS, 386, 407
Lam T. Y., Sheth R. K., 2009, MNRAS, 398, 2143
Lam T. Y., Sheth R. K., Desjacques V., 2009, MNRAS, 399, 1482
Lavaux G., Wandelt B. D., 2012, ApJ, 754, 109
Lewis A., Challinor A., Lasenby A., 2000, ApJ, 538, 473
Li B., 2011, MNRAS, 411, 2615
Li B., Barrow J. D., 2007, Phys. Rev. D, 75, 084010
Li B., Barrow J. D., 2011, Phys. Rev. D, 83, 024007
Li B., Efstathiou G., 2012, MNRAS, 421, 1431
Li B., Lam T. Y., 2012, MNRAS, 425, 730
Li B., Zhao H., 2009, Phys. Rev. D, 80, 044027
Li B., Zhao H., 2010, Phys. Rev. D, 81, 104047
Li B., Zhao G., Teyssier R., Koyama K., 2012a, J. Cosmol. Astropart. Phys., 01, 051
Li B., Zhao G.-B., Koyama K., 2012b, MNRAS, 421, 3481
Lombriser L., Koyama K., Zhao G., Li B., 2012, Phys. Rev. D, 85, 124054
Maggiore M., Riotto A., 2010a, ApJ, 711, 907
Maggiore M., Riotto A., 2010b, ApJ, 717, 515
Melchior P., Sutter P. M., Sheldon E. S., Krause E., Wandelt B. D., 2014, MNRAS, 440, 2922
Mo H. J., White S. D. M., 1996, MNRAS, 282, 347
Musso M., Sheth R. K., 2012, MNRAS, 423, L102
Oyaizu H., 2008, Phys. Rev. D, 78, 123523
Oyaizu H., Lima M., Hu W., 2008, Phys. Rev. D, 78, 123524
Pan D. C., Vogeley M. S., Hoyle F., Choi Y.-Y., Park C., 2012, MNRAS, 421, 926
Paranjape A., Sheth R. K., 2012, MNRAS, 426, 2789
Paranjape A., Lam T. Y., Sheth R. K., 2012a, MNRAS, 420, 1429
Paranjape A., Lam T. Y., Sheth R. K., 2012b, MNRAS, 420, 1648
Paranjape A., Sheth R. K., Desjacques V., 2013, MNRAS, 431, 1503
Planck Collaboration XIX, 2014, A&A, 571, 19
Planck Collaboration XVI, 2014, A&A, 571, 16
Schmidt F., Lima M., Oyaizu H., Hu W., 2009, Phys. Rev. D, 79, 083518
Sheth R. K., 1998, MNRAS, 300, 1057
Sheth R. K., Tormen G., 1999, MNRAS, 308, 119
Sheth R. K., Tormen G., 2002, MNRAS, 329, 61
Sheth R. K., van de Weygaert R., 2004, MNRAS, 350, 517
Sutter P. M., Lavaux G., Wandelt B. D., Weinberg D. H., 2012, ApJ, 761, 187
Sutter P. M., Pisani A., Wandelt B. D., Weinberg D. H., 2014, MNRAS, 443, 2983
Sutter P. M., Carlesi E., Wandelt B. D., Knebe A., 2015, MNRAS, 446, L1
Zentner A. R., 2007, Int. J. Mod. Phys. D, 16, 763
Zhang J., Hui L., 2006, ApJ, 641, 641
Zhao G., Li B., Koyama K., 2011, Phys. Rev. D, 83, 044007

This paper has been typeset from a TEX/LATEX file prepared by the author.